

Salt and Water Transport in Reverse Osmosis Membranes: Beyond the Solution-Diffusion Model

Li Wang, Tianchi Cao, Jouke E. Dykstra, Slawomir Porada, P. M. Biesheuvel, and Menachem Elimelech*



Cite This: *Environ. Sci. Technol.* 2021, 55, 16665–16675



Read Online

ACCESS |



Metrics & More



Article Recommendations



Supporting Information

ABSTRACT: Understanding the salt–water separation mechanisms of reverse osmosis (RO) membranes is critical for the further development and optimization of RO technology. The solution-diffusion (SD) model is widely used to describe water and salt transport in RO, but it does not describe the intricate transport mechanisms of water molecules and ions through the membrane. In this study, we develop an ion transport model for RO, referred to as the solution-friction model, by rigorously considering the mechanisms of partitioning and the interactions among water, salt ions, and the membrane. Ion transport through the membrane is described by the extended Nernst–Planck equation, with the consideration of frictions between the species (i.e., ion, water, and membrane matrix). Water flow through the membrane is governed by the hydraulic pressure gradient and the friction between the water and membrane matrix as well as the friction between water and ions. The model is validated using experimental measurements of salt rejection and permeate water flux in a lab-scale, cross-flow RO setup. We then investigate the effects of feed salt concentration and hydraulic pressure on salt permeability, demonstrating strong dependence of salt permeability on feed salt concentration and applied pressure, starkly disparate from the SD model. Lastly, we develop a framework to analyze the pressure drop distribution across the membrane, demonstrating that cross-membrane transport dominates the overall pressure drop in RO, in marked contrast to the SD model that assumes no pressure drop across the membrane.

KEYWORDS: reverse osmosis, salt permeability, water permeability, ion transport, solution-friction model, solution-diffusion model

Parameter	Solution-Diffusion Model	Solution-Friction Model
Salt permeability 	Constant	Varies with salt concentration and applied pressure
Hydraulic pressure across the membrane 	Constant	Linear decrease
Mechanism of water transport 	Diffusion	Hydraulic pressure gradient
Mechanism of salt transport 	Diffusion	Diffusion + advection + electromigration

INTRODUCTION

Reverse osmosis (RO) is a pressure-driven desalination process that employs a semipermeable membrane for the selective transport of water over salt. Due to its reliability, high energy efficiency, and excellent salt rejection, RO is the dominant desalination technology worldwide.^{1–3} In addition, RO removes a wide range of contaminants from water, rendering it an essential technology for the treatment and reuse of domestic and industrial wastewaters.^{4–7} The driving force for species transport through RO membranes is the gradient of the chemical potential across the membrane in which the applied hydraulic pressure is an important component. Along such gradient, water molecules transport through the membrane, while the transport of salt ions is largely hindered, thereby achieving water–salt selectivity.^{8–10}

At the core of the RO technology is the thin-film composite (TFC) polyamide membrane, which is made by interfacial polymerization.^{1,11,12} Understanding the transport of water and ions through the TFC membrane is critical for improving and optimizing the performance of RO desalination. The solution-diffusion (SD) model is the most widely used theory to describe the separation of water and salt in RO.^{13–15} The SD model assumes that water and salt diffuse through the

membrane polymer matrix independently, with water–salt selectivity or salt separation arising from the differences in the solubility and diffusivity of water and salt through the membrane.

While the SD model with its simple equations has been used extensively to describe salt and water transport in RO process modeling, it does not correctly describe the mechanisms of water and salt transport across the membrane. For example, a recent study using small-angle and quasi-elastic neutron scattering to investigate water transport in desalination membranes indicates that the transport of water molecules is not associated with polymer dynamics, which is a key assumption of the SD model.¹⁶ Instead, the water molecules move freely in continuous water channels that are formed by the polymer network of the membrane. In another recent study, it was shown that the driving force for water transport in

Received: August 23, 2021

Revised: November 8, 2021

Accepted: November 30, 2021

Published: December 8, 2021



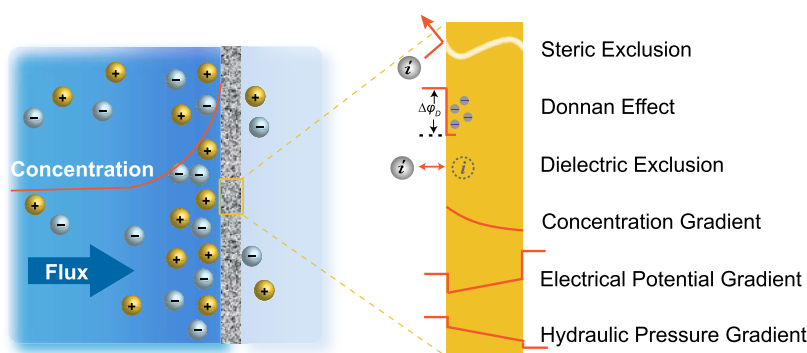


Figure 1. Schematic illustration of water and ion transport through the active layer of RO membranes. The active layer of the membrane comprises a polymer network with continuous, water-filled subnanometer channels/pathways. Salt ions in the membrane are dispersed in the continuous water phase. At the two sides of the membrane (i.e., feed and permeate), salt ions partition into the membrane via three mechanisms: steric exclusion, Donnan effect, and dielectric exclusion. In the feed side of the membrane, the salt concentration increases relative to the feed bulk as a result of concentration polarization. The three salt exclusion mechanisms and the concentration and potential gradient across the membrane are depicted on the right panel.

desalination membranes cannot be by diffusion due to concentration gradient of water within the membrane matrix as implied by the SD model but rather due to hydraulic pressure gradient within the membrane.¹⁷ In addition, several experimental and theoretical studies suggest advective transport of salt, a transport mechanism that is not considered by the SD model.^{9,18} The SD model also considers the partitioning coefficients of water and salt to be constant, which is inconsistent with experimental observations.^{19,20} Lastly, the SD model assumes a uniform distribution of hydraulic pressure within the membrane and that the chemical potential gradient is governed only by the concentration gradient.^{13,14,21}

Over the past decades, significant efforts have been made to develop mechanistic models describing salt exclusion mechanisms and transport of water and salt through RO membranes. A mean-field Donnan-steric pore (DSP) model was developed to account for partitioning by Donnan equilibrium, steric exclusion, and dielectric exclusion.^{22–25} However, the model was mainly used to describe salt rejection or passage without a thorough investigation of the effects of operation conditions and membrane properties on desalination performance. Furthermore, previous studies on the DSP model described the hydraulic pressure drop inside the membrane using the Hagen–Poiseuille equation,^{22,24} neglecting the influence of membrane charge and the resulting electrical potential gradient on the pressure drop across the membrane. These studies further failed to elucidate key transport mechanisms and physicochemical phenomena, such as the resulting distribution of hydraulic pressure across the membrane. Quantification of the pressure distribution across the membrane is important as it is directly related to energy consumption, providing insights and guidance for RO process improvement and membrane fabrication. Therefore, it is imperative to systematically investigate the fundamental physicochemical phenomena that govern the transport of salt and water through RO membranes.

In this study, we elucidate and quantify the complex separation process and transport of salt and water in RO membranes. First, we present an ion/salt transport theory, termed the solution-friction model, that considers the mechanisms of ion partitioning and ion permeation while considering the interactions of water and salt ions with the membrane matrix. RO experiments with varying feed salt concentrations and hydraulic pressures were carried out to

validate the theory. Our theory and experimental observations demonstrate the dependence of salt permeability on salt concentration and hydraulic pressure. Lastly, our analysis provides insights into the hydraulic pressure drop distribution across the membrane. Our results highlight the shortcomings of the SD model and its inability to correctly depict the salt and water transport mechanisms in RO as well as the pressure distribution across the membrane.

MODEL DEVELOPMENT

In our model, we consider the active (selective) layer as the membrane and neglect the impact of the porous support layer on water and salt transport. Unlike the SD model that considers the membrane as a “dense” polymer phase, we view the membrane as a polymer network with continuous, subnanometer water channels/pathways (typically of ~ 0.5 nm^{26,27}). Water in the membrane polymer matrix is in a liquid phase because of the strong tendency of water molecules to adhere to each other, while salt ions are dispersed in water and transport across the membrane through the continuous water phase. Water transport in the membrane is induced by the applied hydraulic pressure.

Ion transport through the membrane active layer is modeled based on the extended Nernst–Planck equation with consideration of solute–membrane friction, while water transport is modeled based on a force balance on water molecules within the membrane. The extended Nernst–Planck equation can be derived from the Maxwell–Stefan theory, which includes the frictions between the various species (i.e., ions, water, and membrane matrix).²⁸ Concentration polarization (CP) is accounted for at the pressurized feed side of the membrane. At both sides of the membrane, partitioning of ions at the membrane–water interface is established. Inside the membrane, ion transport is governed by advection, diffusion, and electromigration.

Salt Partitioning Mechanisms. Before transporting through the membrane, the finite-size-charged ions must partition into the membrane. As shown in Figure 1, three effects are considered at the interface between the membrane and aqueous solution: steric, Donnan, and dielectric.

Steric partitioning is determined by the ratio between the ion radius and pore radius (λ_i). Because ions undergo partial dehydration when partitioning through the membrane,^{29,30} the

Stokes radius is used for the ion size. Assuming spherical ions and cylindrical pores, the partitioning coefficient (Φ_{st}) can be described by^{31,32}

$$\Phi_{st} = (1 - \lambda_i)^2 \quad (1)$$

Donnan equilibrium is established at the membrane–water interface as a result of the membrane charge, allowing ions bearing the opposite charge (i.e., counterions) to preferentially partition into the membrane.^{33–35} This partitioning coefficient, Φ_D , is determined by the Donnan potential at the interface³⁶

$$\Phi_D = \exp(-z_i \Delta \varphi_D) \quad (2)$$

where z_i is the ion charge and $\Delta \varphi_D$ is the dimensionless Donnan potential (i.e., Donnan potential divided by the thermal voltage, 0.0256 V at 25 °C), which is the difference in the potential just inside the membrane and that just outside the membrane. RO membranes are negatively charged;^{34,37} hence, the Donnan potential is negative (i.e., the potential at the interface decreases from just outside to just inside the membrane).

In addition to the steric and Donnan effects, at the interface between water and the membrane, an ion experiences a discontinuity in the dielectric constant.^{38,39} As an ion moves to a membrane medium that has a lower dielectric constant than the aqueous phase, the difference in dielectric constants presents an energy barrier for ion dehydration and partitioning into the membrane.^{40–43} This energy barrier, ΔW_i , can be estimated by the Born model⁴⁴

$$\Delta W_i = \frac{z_i^2 e^2}{8\pi \epsilon_0 r_i} \left(\frac{1}{\epsilon_p} - \frac{1}{\epsilon_b} \right) \quad (3)$$

where e is the elemental charge, ϵ_0 is the vacuum permittivity, r_i is the ion Stokes radius, and ϵ_p and ϵ_b are the dielectric constants of the membrane pore and the bulk solution, respectively. Therefore, the partitioning coefficient for dielectric exclusion can be expressed as^{45,46}

$$\Phi_B = \exp\left(\frac{-\Delta W_i}{k_B T}\right) \quad (4)$$

where k_B and T are the Boltzmann constant and absolute temperature, respectively.

Thus, at the membrane–water interface, the overall equilibrium between ions just outside the membrane, $c_{i,w}$ and ions just inside the membrane, $c_{i,m}$, can be described by

$$c_{i,m} = c_{i,w} \Phi_{st} \Phi_D \Phi_B \quad (5)$$

Here, $c_{i,w}$ is the concentration of ion i at the membrane surface on the feed side.

Several continuum modeling approaches assume that the three partitioning mechanisms are independent of each other.^{23,47,48} However, it is likely that some of these partitioning mechanisms are interrelated. For instance, both steric and dielectric effects are related to the pore size and the ion Stokes radius; hence, the partial dehydration of ions during partitioning into the membrane may be considered in both mechanisms. To date, however, there are no studies or theories about the possible interrelationship between these partitioning mechanisms. Detailed molecular simulations of ion partitioning may shed light on this problem, but it will be very challenging because of the difficulty to accurately depict the chemical

structure of RO membranes in molecular simulations. Hence, we lump $\Phi_{st} \Phi_B$ into a partition coefficient Φ_i resulting in

$$c_{i,m} = c_{i,w} \Phi_i \Phi_D \quad (6)$$

We note that Φ_i is dependent on ion size, but because of the lack of quantitative information on the size of ions inside the membrane after dehydration during partitioning,³⁰ we are using it as a fitting parameter.^{25,49}

Note that $c_{i,w}$ in eqs 5 and 6 is the concentration of ion i near the membrane surface on the feed side, which is different from that in the bulk solution due to concentration polarization (CP). In our model, we approximate the ion concentration near the membrane surface following the boundary layer film model^{50,51}

$$c_{i,w} = c_{i,p} + (c_{i,f} - c_{i,p}) \exp\left(\frac{v_f}{k}\right) \quad (7)$$

where $c_{i,f}$ and $c_{i,p}$ are the concentrations of ion i in the bulk feed solution and in the permeate solution, respectively, v_f is the permeate water flux, and k is the mass transfer coefficient of the CP boundary film. The mass transfer coefficient depends on the hydrodynamic conditions over the membrane surface. The approach for estimating the mass transfer coefficient is summarized in the Supporting Information (Text S1).

Ion Transport through the Membrane. Ion flux across the membrane is generated by the chemical potential gradient, which includes contributions from concentration and electrical potential gradients and the advection of ions by the permeate flow (Figure 1). Inside the RO membrane, we consider the interactions among the various species (i.e., ion–water, water–membrane matrix, and ion–membrane matrix interactions) and include hindrance factors for ion transport. The ion flux is governed by diffusion, electromigration, and advection and can be described by the extended Nernst–Planck equation^{23,25,28}

$$J_i = K_{c,i} c_i v_f - K_{d,i} \epsilon D_i \left(\frac{dc_i}{dx} + z_i c_i \frac{d\varphi}{dx} \right) \quad (8)$$

where J_i is the flux of ion i , $K_{c,i}$ and $K_{d,i}$ are the advective and diffusional hindrance factors, respectively, c_i is the concentration of ion i , v_f is the permeate water velocity, ϵ is the effective membrane porosity, D_i is the bulk ion diffusivity, φ is the dimensionless electrical potential inside the membrane, and x is the dimensionless coordinate through the membrane.

A key difference between eq 8 and the classic Nernst–Planck equation is the inclusion of the hindrance factors, $K_{c,i}$ and $K_{d,i}$. The hindrance factors are derived from hydrodynamic theories that correlate the hindrance factors to the ratio of ion size and pore size.⁵² We note that the hydrodynamic theories are valid for a single spherical ion in a perfect cylindrical pore, which is not appropriate for the polyamide active layer in RO. A recent study suggests that the two hindrance factors (i.e., $K_{c,i}$ and $K_{d,i}$) are identical and can be replaced by one frictional factor or hindrance function, $K_{f,i}$ ⁴⁹ (details in the Text S2, Supporting Information). Therefore, the ion flux can be expressed as

$$J_i = K_{f,i} c_i v_f - K_{f,i} \epsilon D_i \left(\frac{dc_i}{dx} + z_i c_i \frac{d\varphi}{dx} \right) \quad (9)$$

For the negatively charged RO membrane, the electrical potential within the membrane increases in the direction of ion transport, thus reducing the velocity of the cations while enhancing the velocity of the anions.^{53,54} Hence, the flux of

cations is equal to the flux of anions, such that the net charge flux, J_{ch} , is zero (i.e., no current through the membrane)

$$J_{ch} = \sum_i z_i J_i = 0 \quad (10)$$

In addition, throughout the charged membrane, charge neutrality must be satisfied

$$\sum_i z_i c_i + \omega X = 0 \quad (11)$$

where X is the volumetric charge density of the membrane and ω is the sign of the membrane charge (i.e., -1 for the negatively charged RO membrane^{33,34}).

Water Flow and Hydraulic Pressure. The flux of water molecules through the continuous water phase in the membrane is determined by the mechanical forces that act on the water molecules. The total pressure, P^t , acting on a volume element of water is contributed by the hydraulic pressure and osmotic pressure (i.e., $P^t = P - \pi$). The driving force is balanced by the frictions between the membrane matrix and water as well as those between the salt ions and water. Given that the driving force is the gradient of total pressure, the force balance is expressed as^{55,56}

$$\frac{dP^t}{dx} = RTf_{f-m}(v_m - v_f) + RT \sum_i f_{i-f} c_i (v_i - v_f) \quad (12)$$

where R is the gas constant, T is the absolute temperature, v_m and v_i are the velocities of the membrane (zero because it is stationary) and ions, respectively, v_f is the velocity of fluid (water), f_{f-m} is the frictional coefficient between the fluid and membrane, and f_{i-f} is a parameter related to the friction between the ions and the fluid. According to the Einstein relationship^{28,49}

$$f_{i-f} = K_{c,i} / (K_{d,i} D_i) \quad (13)$$

Because $K_{c,i}$ and $K_{d,i}$ are equal, f_{i-f} is simply the inverse of D_i .

To calculate the pressure drop using eq 12, v_i must be determined beforehand. Given that the ion flux J_i (eqs 8 and 9) is the product of c_i and v_i , the latter can be expressed by dividing J_i with c_i

$$v_i = K_{f,i} v_f - K_{f,i} \varepsilon D_i \left(\frac{d \ln c_i}{dx} + z_i \frac{d\phi}{dx} \right) \quad (14)$$

For a given water velocity, v_f , the total pressure drop, and hence the hydraulic pressure drop across the membrane, can be calculated using eqs 12 and 14.

When we neglect the interactions between the ions and membrane pore matrix (i.e., $K_{f,i} = 1$), the hydraulic pressure gradient across the membrane can be simplified to^{28,57}

$$\frac{dP}{dx} + RTf_{f-m} v_f = \omega X RT \frac{d\phi}{dx} \quad (15)$$

Equation 15 indicates that in addition to the friction between the fluid and membrane matrix, f_{f-m} , the electrical potential gradient can also contribute to the hydraulic pressure drop. We note, however, that in this paper, we considered the interactions between ions and the membrane matrix (eq 15 was merely presented to highlight the contribution of the electrical potential gradient). Hence, we calculated the hydraulic pressure drop using eqs 12–14 as discussed above.

When neglecting the frictions between ions and water, the membrane charge and the resulting electrical potential gradient across the membrane (eq 12) can be reduced to a form equivalent to the equation used to describe water flux in the SD model (see the Text S3, Supporting Information). We emphasize that the mechanism of water transport in our model is viscous flow in continuous water channels, rather than diffusion of water due to concentration gradient of water within the membrane polymer, as proposed in the SD model.¹⁷

MATERIALS AND METHODS

Materials and Chemicals. A stock solution of 5 M NaCl was made by dissolving ACS-grade sodium chloride (Fisher Scientific, Pittsburgh, PA) in deionized (DI) water obtained from a Milli-Q ultrapure water purification system (Millipore, Billerica, MA). The stock solution was used to adjust the feed salt concentration. Commercial polyamide thin-film composite RO membrane (SW30XLE, Dow Chemical Company, Midland, MI) was used in our membrane filtration experiments. Before being mounted to the RO test cell, the as-received membrane was wetted by soaking in a solution of 25% v/v isopropanol in DI water for 30 min. The wetted membrane was then thoroughly rinsed with DI water three times and subsequently stored at 4 °C prior to testing.

RO Setup and Experiments. A bench-scale cross-flow RO system was employed to study the performance of the RO membrane under various conditions. The setup has a rectangular plate-and-frame feed flow channel with dimensions of 7.7 cm in length, 2.6 cm in width, and 0.3 cm in height. Thus, the projected membrane area studied was 20 cm². A stainless steel frit is placed on the permeate side.

All experiments were carried out at a cross-flow velocity of 0.21 m s⁻¹ and a temperature of 25.0 ± 0.5 °C. Aliquots of NaCl stock solution were then added to the feed tank to reach the specified feed salt concentration. Three feed concentrations were tested for salt rejections and permeate water fluxes (200, 350, and 600 mM) with the operating pressures varying from 13.8 to 62.1 bar. In these experiments, the membrane was equilibrated with deionized water for 6 h at the specified pressure. After this step, the membrane was equilibrated with the salt solution for 30 min before collecting the permeate samples. The feed tank had a total volume of 5 L, and the permeate was continuously recirculated back to the tank.

Permeate samples were collected in centrifuge tubes, and the solution conductivity was measured with a calibrated conductivity probe (Oakton CON 110, Oakton Instruments, Vernon Hills, IL). The conductivity was then converted to concentration using a predetermined calibration curve. Simultaneously, the permeate water flux was measured with a digital liquid flowmeter (FlowCal 5000, Tovatech, South Orange, NJ). Duplicate tests with different membrane coupons were conducted on the same RO setup to minimize data variance.

Data Analysis. For both experimental and simulated data, the observed salt rejection, R_p , was calculated using the salt concentrations in the feed and permeate

$$R_j = 1 - \frac{c_{i,p}}{c_{i,f}} \quad (16)$$

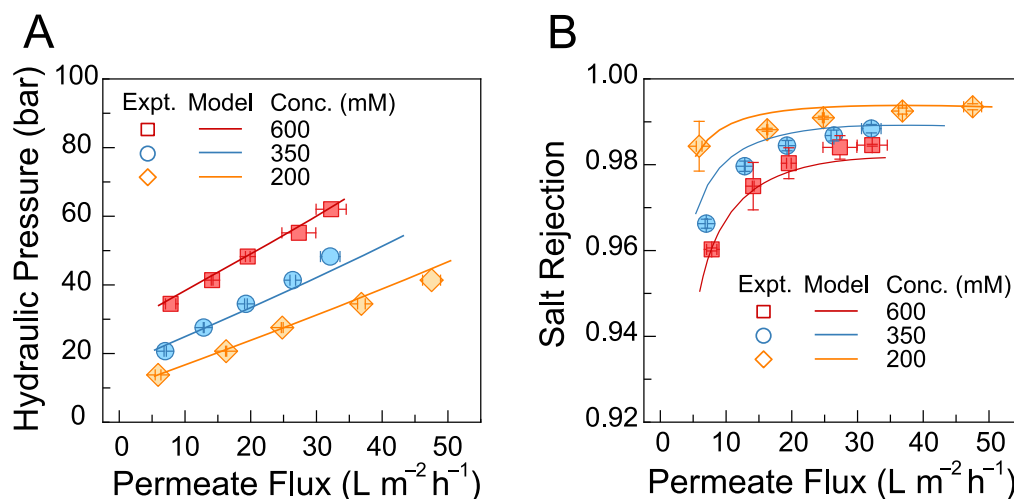


Figure 2. Model validation with experimental data. (A) Hydraulic pressure and (B) salt rejection as a function of permeate water flux at various feed salt concentrations: 200, 350, and 600 mM. The experimental data were collected on a customized cross-flow RO apparatus with a cross-flow velocity of 0.21 m s^{-1} , a temperature of $25.0 \pm 0.5 \text{ }^\circ\text{C}$, and a solution pH of 6.0 ± 0.1 . Open symbols represent the experimental data, and solid curves are generated from the developed model. Other parameters used in the simulations are summarized in Table S1.

where $c_{i,p}$ and $c_{i,f}$ are defined in eq 7. For the 1:1 NaCl salt solution, the ion concentration is the same as the salt concentration in the feed or permeate stream.

For the RO experiments, the salt permeability coefficient, B_{exp} ($\text{L m}^{-2} \text{ h}^{-1}$), was determined from water flux and salt rejection by accounting for concentration polarization

$$B_{\text{exp}} = J_w \left(\frac{1 - R_j}{R_j} \right) \exp \left(-\frac{J_w}{k} \right) \quad (17)$$

where J_w is the permeate water flux ($\text{L m}^{-2} \text{ h}^{-1}$) and k is the experimentally determined mass transfer coefficient ($\text{L m}^{-2} \text{ h}^{-1}$). Specifically, k was measured from the change of water flux after adding salt to the feed tank, which initially contained DI water.⁵⁸ Details on the measurement of the mass transfer coefficient are given in the Supporting Information (Text S1).

For the modeling results, the water permeability coefficient, A ($\text{L m}^{-2} \text{ h}^{-1} \text{ bar}^{-1}$), was calculated by normalizing the permeate water flux, J_w , by the intrinsic driving force across the membrane (i.e., the difference between the hydraulic pressure and the osmotic pressure). The latter requires the estimation of the salt concentration at the membrane surface on the feed side, which is identical to $c_{i,w}$ in eq 7 for a 1:1 salt. Therefore, we arrive at the following equation

$$A = \frac{J_w}{P - 2RT(c_{i,w} - c_{i,p})} \quad (18)$$

The modeling results were also processed to calculate the salt permeability coefficient B_{th}

$$B_{\text{th}} = \frac{c_{i,p} J_w}{c_{i,w} - c_{i,p}} \quad (19)$$

Note that the numerator, $c_{i,p} J_w$, is the salt flux across the membrane.

RESULTS AND DISCUSSION

Model Validation with Experimental Data. A series of RO filtration experiments investigating the effect of feed salt concentration and hydraulic pressure on salt rejection were

conducted to validate the developed model. The experimental data (scattered points) along with the modeling results (solid curves) are presented in Figure 2. We note that only the partition coefficient Φ_i (eq 6) and frictional coefficient f_{f-m} (eq 12) were used as fitting parameters in our model, while the other parameters used, such as membrane charge density,^{34,39} were reported elsewhere for the same type of RO membrane. Details on the parameters used are provided in the Supporting Information (Table S1).

Regardless of the feed salt concentration, the permeate water flux is linearly dependent on hydraulic pressure (Figure 2A). To achieve a larger permeate water flux, a larger hydraulic pressure is needed to drive the water through the membrane. In addition, a more concentrated feed salt solution requires a greater hydraulic pressure to overcome the osmotic pressure difference across the membrane. Salt rejection also depends on the permeate water flux (Figure 2B). A higher salt rejection is typically observed with a greater permeate water flux as the latter dilutes the permeate salt concentration.^{59,60} The observed relationship between salt rejection and water flux is dependent on the feed salt concentration. Specifically, the salt rejection decreases when the feed salt concentration increases because of the increased concentration difference across the membrane and the partitioning of salt ions into the membrane, as we discuss later.

The modeling results predict well the relationship between the permeate water flux and hydraulic pressure, as well as the relationship between the salt rejection and permeate water flux. The good agreement between the experiments and the model predictions highlights the reliability and the predicting power of the developed model. This observation is particularly significant, given that the modeling curves were generated with a single set of physicochemical parameters and only two fitting parameters (Table S1).

Water and Salt Permeabilities. Two phenomenological parameters, water and salt permeabilities, are commonly used to quantify membrane performance in RO. These two parameters are particularly important in the SD model, where they are assumed to be constant and independent of each other. Recent experimental studies, however, suggest that salt permeability may vary with feed salt concentration and

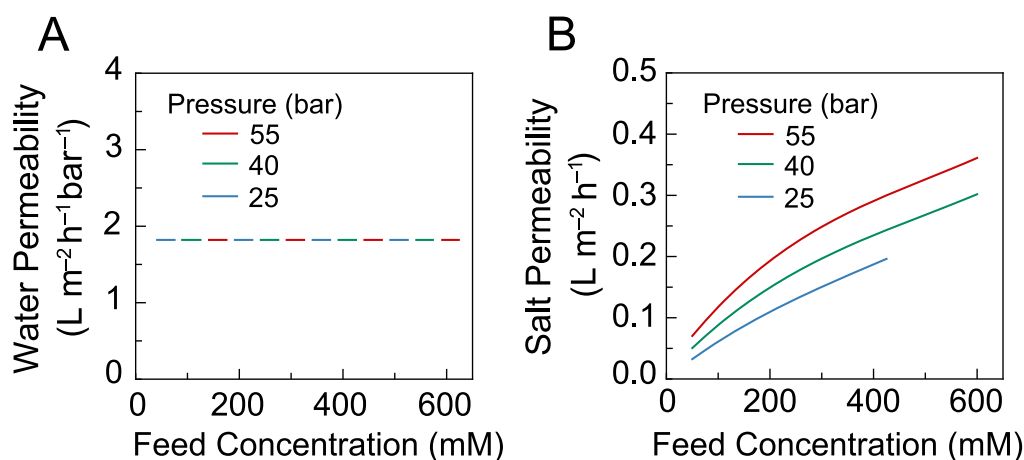


Figure 3. Evaluation of phenomenological parameters for varying feed concentrations and hydraulic pressures: (A) water permeability and (B) salt permeability. Both parameters are calculated from the numerical results generated from the validated model. Specifically, the water permeability is calculated, knowing the hydraulic pressure and the permeate water flux, and the salt permeability is calculated using the salt flux and the concentrations at the two sides of the membrane. Other parameters used in the simulations are summarized in Table S1.

hydraulic pressure.^{18–20} Though our theoretical model does not explicitly use such phenomenological permeabilities, we can calculate the water and salt permeabilities following eqs 18 and 19, respectively, based on the model results for salt rejection and permeate water flux.

Water permeability remains constant at $1.82 \text{ L m}^{-2} \text{ h}^{-1} \text{ bar}^{-1}$ as the salt concentration and hydraulic pressure vary over a wide range (Figure 3A). This observation is attributed to the dominance of the friction between water and the membrane (f_{f-m}) in determining the hydraulic pressure drop across the membrane. Such friction is independent of salt concentration and hydraulic pressure, resulting in stable water permeability regardless of the operating conditions. According to eq 15, the electrical potential gradient across the membrane is expected to influence the hydraulic pressure drop. However, the magnitude of the electrical potential gradient is relatively small because the difference between the effective diffusion coefficients (i.e., $K_{f,i} \epsilon D_i$ in eq 9) of the cations and anions is negligible (i.e., both move at almost similar rates through the membrane, thus forming a small electric potential gradient).

Salt permeability changes significantly with feed salt concentration (Figure 3B). Specifically, increasing the feed salt concentration elevates the salt concentration near the membrane surface, thereby decreasing the magnitude of the Donnan potential at the interface between the feed solution and membrane. As a result, the partitioning of co-ions (i.e., Cl^-) increases significantly at the interface between the membrane and feed solution because of the exponential relationship between the partitioning coefficient and Donnan potential (eq 2). The increased concentration gradient of co-ions enhances the salt flux as the latter is governed by the co-ion flux. In addition, the increase of salt flux (i.e., numerator of eq 19) outpaces the increase of salt concentration difference across the membrane (i.e., the denominator of eq 19). Consequently, the salt permeability increases with feed salt concentration.

The applied hydraulic pressure influences the salt permeability as well. Specifically, for a given feed salt concentration, increasing the hydraulic pressure results in a higher water flux, thereby increasing the salt concentration near the membrane (eq 7) and the advective salt flux across the membrane (eqs 8 and 9). Consequently, the permeate salt concentration

increases. The increase in permeate salt concentration and water flux (i.e., the numerator in eq 19) outpaces the increase in salt concentration difference across the membrane (i.e., denominator of eq 19), resulting in an increased salt permeability with an increasing hydraulic pressure. The influence of hydraulic pressure on salt permeability is more evident at higher feed concentrations, resulting from the increased partitioning of ions into the membrane and thereby enhanced salt flux (via both advection and diffusion).

The SD model assumes that the salt permeability coefficient is independent of feed salt concentration and applied pressure. Our modeling results, however, show that salt permeability increases significantly with increasing feed salt concentration and to a lesser extent with increasing hydraulic pressure. This observation is consistent with recent experimental observations of higher salt permeability coefficients at higher feed salt concentrations and applied pressures.^{18–20} Our results clearly show that the inclusion of the detailed mechanisms for salt transport in RO modeling is critical to reconcile the inadequacy of the SD model to describe experimental observations of salt transport.

Experimental Verification of Variation of Salt Permeability with Operating Conditions. To further demonstrate the dependence of salt permeability on operating conditions, we determined the salt permeability based on the experimental data presented in Figure 2. Salt permeability is highly dependent on the feed salt concentration (Figure 4A). Specifically, an increase in feed salt concentration enhances salt partitioning into the membrane and thus the salt flux, resulting in increased salt permeability. The influence of feed salt concentration on salt permeability has been discussed in detail in the previous section when we described the model predictions (Figure 3B). Salt permeability also depends on the permeate water flux but to a lesser extent. For instance, when the feed salt concentration is 350 mM, salt permeability slightly increases from 0.225 to 0.246 $\text{L m}^{-2} \text{ h}^{-1}$ (9.35% increase) as the permeate water flux increases from 12.9 to 32.1 $\text{L m}^{-2} \text{ h}^{-1}$. Our results suggest that diffusive transport contributes significantly more than advective transport to the salt flux through the membrane.

The developed model predicts a strong dependence of salt permeability on feed salt concentration (Figure 4A, solid

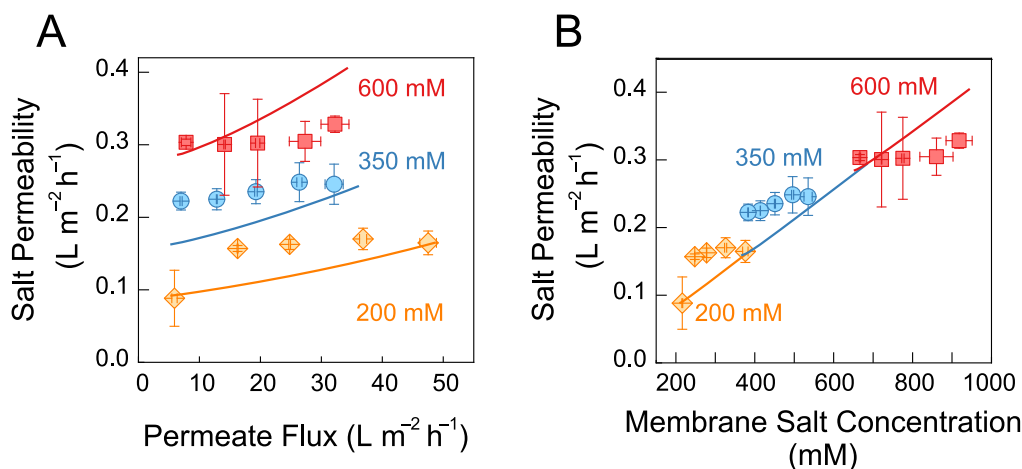


Figure 4. Dependence of salt permeability on (A) permeate water flux and (B) salt concentration at the membrane surface as calculated from eq 7. RO experiments were conducted with a customized cross-flow apparatus at various feed salt concentrations and permeate water fluxes (the latter was controlled by varying the applied hydraulic pressure). All experiments were carried out at a cross-flow velocity of 0.21 m s^{-1} , a solution pH of 6.0 ± 0.1 , and a temperature of $25.0 \pm 0.5 \text{ }^\circ\text{C}$. The solid lines are predictions based on the solution-friction model (model parameters are summarized in Table S1).

lines). In addition, the model captures the relatively weaker influence of permeate water flux on salt permeability. As shown in Figure 4A, the model slightly overestimates the effect of permeate water flux at the high feed salt concentration (i.e., 600 mM). We suggest that salt rejection may be slightly enhanced due to membrane compaction at the high pressure (up to 62 bar) used for the experiments at a 600 mM feed salt concentration and high water fluxes.

Salt concentration at the membrane surface is elevated by the permeate water flux due to concentration polarization. Here, we examine the influence of salt concentration at the membrane surface on the salt permeability. As shown in Figure 4B, the salt permeability has a linear relationship with the salt concentration at the membrane surface, regardless of the feed salt concentration. Notably, the model predictions for the dependence of salt permeability on salt concentration at the membrane surface converge to a single line, which well matches the trend of the experimental data. Our experimental and modeling results highlight the strong dependence of salt permeability on operating conditions and the inadequacy of the SD model, which assumes a constant salt permeability.

Pressure Distribution across the Membrane. The pressure across the membrane in the SD model is assumed to be constant, extending from the feed solution to the interface between the membrane and permeate solution. In this section, we will re-examine this assumption based on the solution-friction theory for salt and water transport presented in the paper.

As we described in the Model Development section, the driving force for water flux through the membrane is the gradient of total pressure, P^t . The latter can be alternatively expressed in terms of the chemical potential (details in the Supporting Information, Text S4). P^t is continuous from the feed solution, across the membrane, and to the permeate solution. Therefore, P^t just inside the membrane and P^t in solution just outside the membrane at the membrane–solution interfaces are equal, resulting in the following expressions

$$P_{aq}^f - \pi_{aq}^f = P_m^f - \pi_m^f \quad (20a)$$

$$P_{aq}^p - \pi_{aq}^p = P_m^p - \pi_m^p \quad (20b)$$

where P_{aq}^f and π_{aq}^f are the hydraulic pressure and osmotic pressure in the feed solution just outside the membrane, P_m^f and π_m^f are the hydraulic pressure and osmotic pressure just inside the membrane at the interface between the feed solution and membrane, P_{aq}^p and π_{aq}^p are the hydraulic pressure and osmotic pressure in the permeate solution, and P_m^p and π_m^p are the hydraulic pressure and osmotic pressure just inside the membrane at the interface between the permeate solution and membrane, respectively. Note that P_{aq}^f is the hydraulic pressure applied to the feed solution to drive the transport of water in RO.

Inspection of eq 20a reveals that the assumption of constant hydraulic pressure within the membrane in the SD model is self-contradictory. Specifically, the SD model assumes P_{aq}^f is equal to P_m^f , implying that salt concentration in the feed solution at the membrane interface should be equal to that within the membrane (i.e., $\pi_{aq}^f = \pi_m^f$ as obtained from eq 20a). This relationship suggests that the RO membrane does not exclude salt ions, in conflict with the salt partitioning mechanism of the SD model.

Before applying the hydraulic pressure at the saline feed solution (i.e., $P_{aq}^f = 0$), P_m^f is negative due to the partitioning of salt at the interface (i.e., $\pi_m^f < \pi_{aq}^f$ in eq 20a). On the permeate side, if pure water is present, then both π_{aq}^p and π_m^p are zero. In addition, because the permeate solution is not pressurized, P_{aq}^p and P_m^p are zero as well. Therefore, inside the membrane, P_m^p is larger than P_m^f , driving the water flow from the permeate side to the feed side (Figure S1), similar to observations in forward osmosis. This analysis suggests that the driving force in osmosis is a hydraulic pressure gradient and that the membrane in osmosis is under negative hydraulic pressure, as shown in a recent study.¹⁷

Upon applying hydraulic pressure to the feed solution ($P_{aq}^f > 0$), P_m^f increases accordingly (Figure 5A). Importantly, the hydraulic pressure experiences jumps at the two interfaces between the membrane and aqueous solution, resulting from salt exclusion/partitioning (i.e., $\pi_{aq} \neq \pi_m$ in eqs 20a and 20b). The two jumps correspond to the hydraulic pressure drops as water molecules enter (P_{entry}) and exit the membrane (P_{exit}), respectively. Furthermore, the hydraulic pressure decreases as the water molecules move through the membrane pores from

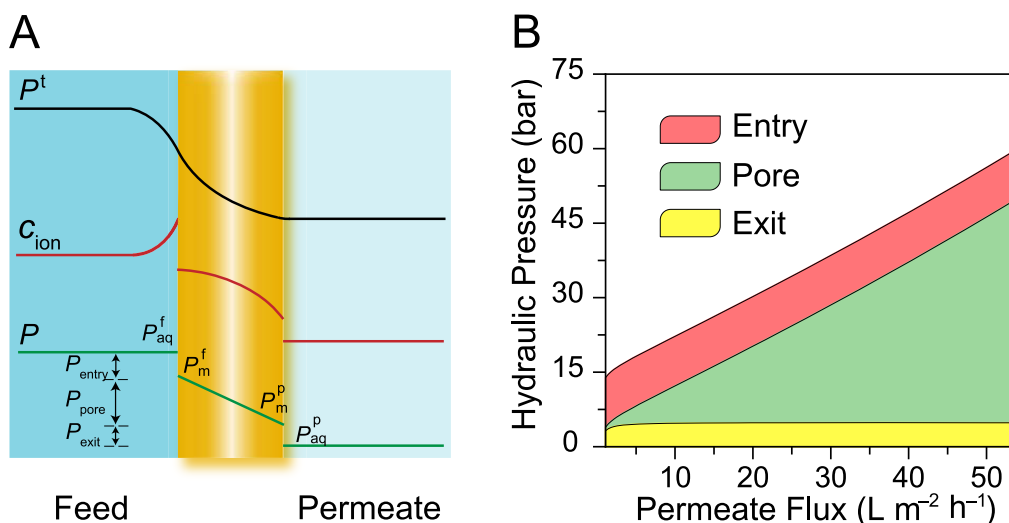


Figure 5. (A) Schematic diagram depicting the total pressure, ion concentration, and hydraulic pressure distribution across the membrane. (B) Modeled breakdown of the three pressure drops as a function of permeate water flux. For the modeling results in (B), the feed concentration is set as 300 mM while varying the permeate water flux. The color-coded regions represent the pressure drops: P_{entry} (red), P_{pore} (green), and P_{exit} (yellow). Other parameters used in the model are summarized in Table S1.

the feed side to the permeate side (P_{pore}). These three pressure drops are equal to the hydraulic pressure applied to the feed solution in RO (Figure 5A). The three pressure drops are hydraulic pressure differences expressed as

$$P_{entry} = P_{aq}^f - P_m^f \quad (21a)$$

$$P_{pore} = P_m^f - P_m^p \quad (21b)$$

$$P_{exit} = P_m^p - P_{aq}^p \quad (21c)$$

Quantification of these pressure drops is critical to evaluating the energy dissipations along the pathway of water transport in RO. According to eq 21a, we must calculate the hydraulic pressures at the two interfaces just inside the membrane before quantifying the pressure drops. Combining eqs 20a and 21a, we obtain that P_{entry} and P_{exit} are related to the osmotic pressures in the solution and just inside the membrane at the corresponding interfaces

$$P_{entry} = \pi_{aq}^f - \pi_m^f \quad (22a)$$

$$P_{exit} = \pi_m^p - \pi_{aq}^p \quad (22b)$$

Such osmotic pressures are related to the corresponding salt concentrations within the membrane, which can be obtained from the model results. Further, P_{pore} , the hydraulic pressure difference across the membrane, can be calculated by eq 12. Therefore, all the pressure drops can be quantified with our ion transport model.

A typical distribution of hydraulic pressure as a function of permeate water flux is shown in Figure 5B. Increasing permeate water flux increases the salt concentration near the membrane surface due to concentration polarization, subsequently increasing π_{aq}^f . The increase in salt concentration also increases the salt partitioning in the membrane, which increases π_m^f . Because π_{aq}^f and π_m^f increase at a similar pace with increasing permeate water flux, P_{entry} does not change with permeate water flux (eq 22a). On the permeate side, the aqueous salt concentration remains very low and is insensitive to the permeate flux because of the high salt rejection (Figure 2B).

Hence, the salt concentration difference across the interface between the permeate solution and the membrane, and P_{exit} remain unchanged (eq 22b). On the other hand, the pressure drop across the membrane, P_{pore} , strongly depends on the permeate water flux, primarily due to the friction between the water molecules and the membrane matrix (eq 12). Because the friction between the water molecules and the membrane is proportional to the permeate water flux, P_{pore} increases linearly with permeate water flux.

Transmembrane Transport Dominates Overall Hydraulic Pressure Drop. To identify the dominant step for hydraulic pressure dissipation, we further calculate the percent contribution of each pressure drop to the overall applied hydraulic pressure difference across the membrane. In Figure 6A, we analyze the percent pressure drop contribution as a function of permeate water flux. As discussed in the previous paragraph, P_{entry} is insensitive to permeate water flux (Figure 5B). However, because a greater hydraulic pressure is required to achieve a larger water flux, the percent contribution of P_{entry} decreases. Similarly, the contribution of P_{exit} to the total hydraulic pressure decreases as well when the permeate water flux increases. In contrast, the percent contribution of P_{pore} increases steadily, dominating the hydraulic pressure losses, especially when achieving a relatively large permeate water flux. For example, when a permeate water flux of $36 L m^{-2} h^{-1}$ is achieved, 66.1% of the hydraulic pressure is expended to transport the water through the membrane pores (i.e., P_{pore}), while P_{entry} contributes a much smaller portion of the total hydraulic pressure (i.e., 22.9%).

In addition, we analyze the percent contribution of each pressure drop to the overall applied hydraulic pressure as a function of feed salt concentrations in Figure 6B. As discussed earlier, increasing the feed salt concentration elevates the ion concentration inside the membrane and therefore π_m^f . Notably, for a given permeate water flux, the salt concentration near the membrane surface has an exponential relationship with the feed salt concentration (eq 7). Therefore, the increase of π_{aq}^f outpaces the increase of π_m^f , resulting in an increased P_{entry} (eq 22a) as well as its percent contribution to the total hydraulic pressure. On the permeate side, the salt concentration is

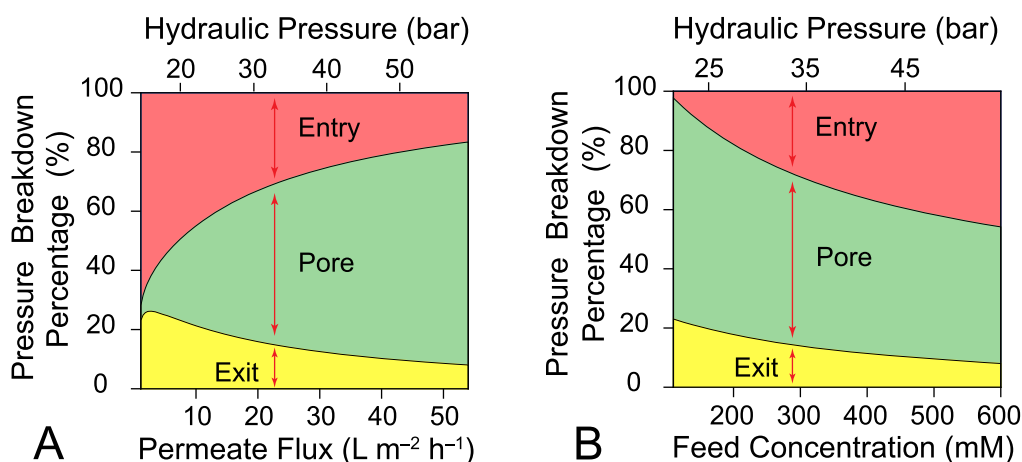


Figure 6. Pressure breakdown percentage as a function of (A) permeate water flux and (B) feed salt concentration. The percentages of the three pressure drops are modeled for the following conditions: in (A), a feed concentration of 300 mM while varying permeate water flux (via the applied hydraulic pressure); in (B), a permeate water flux of 25.2 L m⁻² h⁻¹ while varying feed salt concentration and the corresponding hydraulic pressure (to maintain a fixed water flux). Other parameters used in the model are summarized in Table S1. In both panels, the total hydraulic pressures are calculated accordingly and shown as the horizontal axes above.

minimal (i.e., very small π_{aq}^p), leading to a small π_m^p and thus a relatively small P_{exit} (eq 22b). However, a greater hydraulic pressure is needed to achieve a given permeate water flux when the feed salt concentration is higher, diminishing the percent contribution of P_{exit} . Inside the membrane pores, P_{pore} remains the same, as it primarily depends on the friction between the permeate water flux (constant in Figure 6B) and membrane matrix. Therefore, the percent contribution of P_{pore} decreases as the total hydraulic pressure increases with increasing feed salt concentration. Nevertheless, P_{pore} dominates the overall hydraulic pressure drop for a wide range of feed salt concentrations.

■ IMPLICATIONS

We presented a coupled salt and water transport theory for RO—the solution-friction model—by considering the various mechanisms of salt partitioning and the interactions among ions, water, and the membrane pore matrix. Our model, supported by experimental observations, predicts strong dependence of salt permeability on feed salt concentration and to a lesser extent on hydraulic pressure (or water flux). This behavior is in marked contrast to the commonly used SD model, which assumes constant salt permeability, independent of feed salt concentration and hydraulic pressure.

Unlike the SD model that assumes diffusive water transport induced by the concentration gradient of water within the membrane polymer matrix, our model considers water flow in interconnected, water-filled subnanometer channels/pores induced by the hydraulic pressure gradient. Within the framework of our model, we determined the distribution of hydraulic pressure across the membrane, revealing a linear pressure drop within the membrane. Notably, the obtained hydraulic pressure profile within the membrane is in stark contradiction to the SD model, which assumes a nonphysical, constant hydraulic pressure across the membrane.

The theoretical and experimental verification of the dependence of salt permeability on operating conditions (feed salt concentration and permeate water flux) has important implications for the characterization of RO membranes and for the use of the SD model for process modeling. One important implication is that the salt

permeability coefficient, which is currently determined by an RO experiment under pressure, is not an intrinsic property of the membrane as currently assumed, but rather a parameter that is also influenced by operation conditions (feed salt concentration and applied pressure). It is therefore necessary to standardize the conditions for reporting salt permeability coefficients.

Current modeling approaches treat the RO membrane as a “dense” polymer phase or a “black box”, which limits our understanding of water and salt transport mechanisms in RO and hinders further progress in membrane development. Our proposed solution-friction model presents a mechanistic approach to describe water and salt flux in RO membranes, analogous to the progress made in the mechanistic description of ion transport in ion-exchange membranes in electrodialysis. Because of the complex chemical structure of RO membranes, several of the parameters used in the solution-friction model were determined from fitting to experimental data. With the advent of molecular simulations and machine learning, we expect that several such parameters can be obtained theoretically once we can more accurately depict the chemical and physical structures of RO membranes.

■ ASSOCIATED CONTENT

SI Supporting Information

The Supporting Information is available free of charge at <https://pubs.acs.org/doi/10.1021/acs.est.1c05649>.

Estimation of the mass transfer coefficient in the boundary layer (Text S1); relationship between the hindrance factors and frictional factor (Text S2); derivation of water flux equation equivalent to the SD model (Text S3); expression of the total pressure based on chemical potential (Text S4); parameters used in the solution-friction model (Table S1); and schematic profiles of the chemical potential, salt concentration, and pressure when no hydraulic pressure is applied on the feed solution (Figure S1) (PDF)

AUTHOR INFORMATION

Corresponding Author

Menachem Elimelech – Department of Chemical and Environmental Engineering, Yale University, New Haven, Connecticut 06520-8286, United States; orcid.org/0000-0003-4186-1563; Phone: +1 (203) 432-2789; Email: menachem.elimelech@yale.edu

Authors

Li Wang – Department of Chemical and Environmental Engineering, Yale University, New Haven, Connecticut 06520-8286, United States; orcid.org/0000-0002-5542-6696

Tianchi Cao – Department of Chemical and Environmental Engineering, Yale University, New Haven, Connecticut 06520-8286, United States

Jouke E. Dykstra – Environmental Technology, Wageningen University, 6708 WG Wageningen, The Netherlands; orcid.org/0000-0002-0377-4779

Slawomir Porada – Wetsus, European Centre of Excellence for Sustainable Water Technology, 8911 MA Leeuwarden, The Netherlands; orcid.org/0000-0002-9709-2401

P. M. Biesheuvel – Wetsus, European Centre of Excellence for Sustainable Water Technology, 8911 MA Leeuwarden, The Netherlands; orcid.org/0000-0002-5468-559X

Complete contact information is available at: <https://pubs.acs.org/10.1021/acs.est.1c05649>

Author Contributions

The manuscript was written through contributions of all authors. All authors have given approval to the final version of the manuscript.

Notes

The authors declare no competing financial interest.

ACKNOWLEDGMENTS

This work was supported by CENT, an Energy Frontier Research Center funded by the U.S. Department of Energy, Office of Science, Basic Energy Sciences, under Award No. DESC0019112.

REFERENCES

- (1) Elimelech, M.; Phillip, W. A. The Future of Seawater Desalination: Energy, Technology, and the Environment. *Science* **2011**, *333*, 712–717.
- (2) Fritzmann, C.; Lowenberg, J.; Wintgens, T.; Melin, T. State-of-the-art of reverse osmosis desalination. *Desalination* **2007**, *216*, 1–76.
- (3) Cohen, Y.; Semiat, R.; Rahardianto, A. A perspective on reverse osmosis water desalination: Quest for sustainability. *AIChE J.* **2017**, *63*, 1771–1784.
- (4) Bernados, B. Reverse Osmosis for Direct Potable Reuse in California. *J. – Am. Water Works Assoc.* **2018**, *110*, 28–36.
- (5) Al-Rifai, J. H.; Khabbaz, H.; Schafer, A. I. Removal of pharmaceuticals and endocrine disrupting compounds in a water recycling process using reverse osmosis systems. *Sep. Purif. Technol.* **2011**, *77*, 60–67.
- (6) Vourch, M.; Balanec, B.; Chaufer, B.; Dorange, G. Treatment of dairy industry wastewater by reverse osmosis for water reuse. *Desalination* **2008**, *219*, 190–202.
- (7) Lu, D. N.; Sha, S.; Luo, J. Y.; Huang, Z. R.; Jackie, X. Z. Treatment train approaches for the remediation of per- and polyfluoroalkyl substances (PFAS): A critical review. *J. Hazard. Mater.* **2020**, *386*, No. 121963.
- (8) Wang, L.; Violet, C.; DuChanois, R. M.; Elimelech, M. Derivation of the Theoretical Minimum Energy of Separation of Desalination Processes. *J. Chem. Educ.* **2020**, *97*, 4361–4369.
- (9) Kedem, O.; Katchalsky, A. Thermodynamic Analysis of the Permeability of Biological Membranes to Non-Electrolytes. *Biochim. Biophys. Acta* **1958**, *27*, 229–246.
- (10) Sasidhar, V.; Ruckenstein, E. Electrolyte Osmosis through Capillaries. *J. Colloid Interface Sci.* **1981**, *82*, 439–457.
- (11) Werber, J. R.; Osuji, C. O.; Elimelech, M. Materials for next-generation desalination and water purification membranes. *Nat. Rev. Mater.* **2016**, *1*, No. 16018.
- (12) Tan, Z.; Chen, S. F.; Peng, X. S.; Zhang, L.; Gao, C. J. Polyamide membranes with nanoscale Turing structures for water purification. *Science* **2018**, *360*, 518.
- (13) Wijmans, J. G.; Baker, R. W. The Solution-Diffusion Model - a Review. *J. Membr. Sci.* **1995**, *107*, 1–21.
- (14) Baker, R. W. *Membrane Technology and Applications*, 3rd ed.; Wiley, 2012.
- (15) Paul, D. R. Reformulation of the solution-diffusion theory of reverse osmosis. *J. Membr. Sci.* **2004**, *241*, 371–386.
- (16) Chan, E. P.; Frieberg, B. R.; Ito, K.; Tarver, J.; Tyagi, M.; Zhang, W. X.; Coughlin, E. B.; Stafford, C. M.; Roy, A.; Rosenberg, S.; Soles, C. L. Insights into the Water Transport Mechanism in Polymeric Membranes from Neutron Scattering. *Macromolecules* **2020**, *53*, 1443–1450.
- (17) Song, L.; Heiranian, M.; Elimelech, M. True driving force and characteristics of water transport in osmotic membranes. *Desalination* **2021**, *520*, No. 115360.
- (18) Roy, Y.; Lienhard, J. H. On the presence of solute-solvent transport coupling in reverse osmosis. *J. Membr. Sci.* **2020**, *611*, No. 118272.
- (19) Jang, E. S.; Mickols, W.; Sujanani, R.; Helenic, A.; Dilenschneider, T. J.; Kamecev, J.; Paul, D. R.; Freeman, B. D. Influence of concentration polarization and thermodynamic non-ideality on salt transport in reverse osmosis membranes. *J. Membr. Sci.* **2019**, *572*, 668–675.
- (20) Straub, A. P.; Osuji, C. O.; Cath, T. Y.; Elimelech, M. Selectivity and Mass Transfer Limitations in Pressure-Retarded Osmosis at High Concentrations and Increased Operating Pressures. *Environ. Sci. Technol.* **2015**, *49*, 12551–12559.
- (21) Paul, D. R. The role of membrane pressure in reverse osmosis. *J. Appl. Polym. Sci.* **1972**, *16*, 771–782.
- (22) Geraldes, V.; Alves, A. M. B. Computer program for simulation of mass transport in nanofiltration membranes. *J. Membr. Sci.* **2008**, *321*, 172–182.
- (23) Zhang, L.; Hamelers, H. V. M.; Biesheuvel, P. M. Modeling permeate pH in RO membranes by the extended Donnan steric model. *J. Membr. Sci.* **2020**, *613*, No. 118511.
- (24) Wang, R. Y.; Lin, S. H. Pore model for nanofiltration: History, theoretical framework, key predictions, limitations, and prospects. *J. Membr. Sci.* **2021**, *620*, No. 118809.
- (25) Biesheuvel, P. M.; Zhang, L.; Gasquet, P.; Blankert, B.; Elimelech, M.; van der Meer, W. G. J. Ion Selectivity in Brackish Water Desalination by Reverse Osmosis: Theory, Measurements, and Implications. *Environ. Sci. Technol. Lett.* **2020**, *7*, 42–47.
- (26) Davenport, D. M.; Ritt, C. L.; Verbeke, R.; Dickmann, M.; Egger, W.; Vankelecom, I. F. J.; Elimelech, M. Thin film composite membrane compaction in high-pressure reverse osmosis. *J. Membr. Sci.* **2020**, *610*, No. 118268.
- (27) Chu, K. H.; Mang, J. S.; Lim, J.; Hong, S.; Hwang, M. H. Variation of free volume and thickness by high pressure applied on thin film composite reverse osmosis membrane. *Desalination* **2021**, *520*, No. 115365.
- (28) Oren, Y. S.; Biesheuvel, P. M. Theory of Ion and Water Transport in Reverse-Osmosis Membranes. *Phys. Rev. Appl.* **2018**, *9*, No. 024034.
- (29) Richards, L. A.; Schafer, A. I.; Richards, B. S.; Corry, B. The Importance of Dehydration in Determining Ion Transport in Narrow Pores. *Small* **2012**, *8*, 1701–1709.

- (30) Lu, C. H.; Hu, C. Z.; Ritt, C. L.; Hua, X.; Sun, J. Q.; Xia, H. L.; Liu, Y. Y.; Li, D. W.; Ma, B. W.; Elimelech, M.; Qu, J. H. In Situ Characterization of Dehydration during Ion Transport in Polymeric Nanochannels. *J. Am. Chem. Soc.* **2021**, *143*, 14242–14252.
- (31) Deen, W. M. Hindered Transport of Large Molecules in Liquid-Filled Pores. *AIChE J.* **1987**, *33*, 1409–1425.
- (32) Bowen, W. R.; Mohammad, A. W. Diafiltration by nanofiltration: Prediction and optimization. *AIChE J.* **1998**, *44*, 1799–1812.
- (33) Childress, A. E.; Elimelech, M. Relating nanofiltration membrane performance to membrane charge (electrokinetic) characteristics. *Environ. Sci. Technol.* **2000**, *34*, 3710–3716.
- (34) Coronell, O.; Marinas, B. J.; Zhang, X. J.; Cahill, D. G. Quantification of functional groups and modeling of their ionization behavior in the active layer of FT30 reverse osmosis membrane. *Environ. Sci. Technol.* **2008**, *42*, S260–S266.
- (35) Bruni, L.; Bandini, S. The role of the electrolyte on the mechanism of charge formation in polyamide nanofiltration membranes. *J. Membr. Sci.* **2008**, *308*, 136–151.
- (36) Chaudhury, S. G. The Donnan membrane equilibrium. *Nature* **1943**, *152*, 76–77.
- (37) Childress, A. E.; Elimelech, M. Effect of solution chemistry on the surface charge of polymeric reverse osmosis and nanofiltration membranes. *J. Membr. Sci.* **1996**, *119*, 253–268.
- (38) Ding, M. X.; Ghoufi, A.; Szymczyk, A. Molecular simulations of polyamide reverse osmosis membranes. *Desalination* **2014**, *343*, 48–53.
- (39) Ritt, C. L.; Werber, J. R.; Wang, M. Y.; Yang, Z. Y.; Zhao, Y. M.; Kulik, H. J.; Elimelech, M. Ionization behavior of nanoporous polyamide membranes. *Proc. Natl. Acad. Sci. U.S.A.* **2020**, *117*, 30191–30200.
- (40) Yaroshchuk, A. E. Dielectric exclusion of ions from membranes. *Adv. Colloid Interface Sci.* **2000**, *85*, 193–230.
- (41) Bandini, S.; Vezzani, D. Nanofiltration modeling: the role of dielectric exclusion in membrane characterization. *Chem. Eng. Sci.* **2003**, *58*, 3303–3326.
- (42) Liu, X. J.; Lu, B. Z. Incorporating Born solvation energy into the three-dimensional Poisson-Nernst-Planck model to study ion selectivity in KcsA K⁺ channels. *Phys. Rev. E* **2017**, *96*, No. 062416.
- (43) Croxton, T.; Mcquarrie, D. A.; Patey, G. N.; Torrie, G. M.; Valleau, J. P. Ionic Solution near an Uncharged Surface with Image Forces. *Can. J. Chem.* **1981**, *59*, 1998–2003.
- (44) Born, M. Volumen und Hydratationswärme der Ionen. *Z. Phys.* **1920**, *1*, 45–48.
- (45) Oatley, D. L.; Llenas, L.; Perez, R.; Williams, P. M.; Martinez-Llado, X.; Rovira, M. Review of the dielectric properties of nanofiltration membranes and verification of the single oriented layer approximation. *Adv. Colloid Interface Sci.* **2012**, *173*, 1–11.
- (46) Guzmán-García, A. G.; Pintauro, P. N.; Verbrugge, M. W.; Hill, R. F. Development of a Space-Charge Transport Model for Ion-Exchange Membranes. *AIChE J.* **1990**, *36*, 1061–1074.
- (47) Freger, V. Ion partitioning and permeation in charged low-*T** membranes. *Adv. Colloid Interface Sci.* **2020**, *277*, No. 102107.
- (48) Yaroshchuk, A.; Bruening, M. L.; Zholkovskiy, E. Modelling nanofiltration of electrolyte solutions. *Adv. Colloid Interface Sci.* **2019**, *268*, 39–63.
- (49) Biesheuvel, P. M.; Porada, S.; Elimelech, M.; Dykstra, J. E. Tutorial review of Reverse Osmosis and Electrodialysis. 2021, arXiv:2110.07506. arXiv.org e-Print archive. <https://arxiv.org/abs/2110.07506>.
- (50) Werber, J. R.; Deshmukh, A.; Elimelech, M. The Critical Need for Increased Selectivity, Not Increased Water Permeability, for Desalination Membranes. *Environ. Sci. Technol. Lett.* **2016**, *3*, 112–120.
- (51) Gerald, V.; Afonso, M. D. Prediction of the concentration polarization in the nanofiltration/reverse osmosis of dilute multi-ionic solutions. *J. Membr. Sci.* **2007**, *300*, 20–27.
- (52) Dechadilok, P.; Deen, W. M. Hindrance factors for diffusion and convection in pores. *Ind. Eng. Chem. Res.* **2006**, *45*, 6953–6959.
- (53) Wang, L.; Wang, Z.; Patel, S. K.; Lin, S.; Elimelech, M. Nanopore-Based Power Generation from Salinity Gradient: Why It Is Not Viable. *ACS Nano* **2021**, *15*, 4093–4107.
- (54) Zhang, L.; Biesheuvel, P. M.; Ryzhkov, I. I. Theory of Ion and Water Transport in Electron-Conducting Membrane Pores with pH-Dependent Chemical Charge. *Phys. Rev. Appl.* **2019**, *12*, No. 014039.
- (55) Biesheuvel, P. M. Two-fluid model for the simultaneous flow of colloids and fluids in porous media. *J. Colloid Interface Sci.* **2011**, *355*, 389–395.
- (56) Biesheuvel, P. M.; Dykstra, J. E. *Physics of Electrochemical Processes*, 2020.
- (57) de Lint, W. B. S.; Biesheuvel, P. M.; Verweij, H. Application of the charge regulation model to transport of ions through hydrophilic membranes: One-dimensional transport model for narrow pores (nanofiltration). *J. Colloid Interface Sci.* **2002**, *251*, 131–142.
- (58) Sutzkover, I.; Hasson, D.; Semiat, R. Simple technique for measuring the concentration polarization level in a reverse osmosis system. *Desalination* **2000**, *131*, 117–127.
- (59) Takeuchi, K.; Takizawa, Y.; Kitazawa, H.; Fujii, M.; Hosaka, K.; Ortiz-Medina, J.; Morelos-Gomez, A.; Cruz-Silva, R.; Fujishige, M.; Akuzawa, N.; Endo, M. Salt rejection behavior of carbon nanotube-polyamide nanocomposite reverse osmosis membranes in several salt solutions. *Desalination* **2018**, *443*, 165–171.
- (60) Henkens, W. C. M.; Smit, J. A. M. Salt Rejection and Flux in Reverse-Osmosis with Compactible Membranes. *Desalination* **1979**, *28*, 65–85.